

1 **High-level cognition during story listening is reflected in
2 high-order dynamic correlations in neural activity patterns**

3 Lucy L. W. Owen¹, Thomas H. Chang^{1,2}, and Jeremy R. Manning^{1,†}

¹Department of Psychological and Brain Sciences,
Dartmouth College, Hanover, NH

²Amazon.com, Seattle, WA

[†]Address correspondence to jeremy.r.manning@dartmouth.edu

4 October 20, 2020

5 **Abstract**

6 Our thoughts arise from coordinated patterns of interactions between brain structures that change with
7 our ongoing experiences. High-order dynamic correlations in neural activity patterns reflect different
8 subgraphs of the brain’s connectome that display homologous lower-level dynamic correlations. We tested
9 the hypothesis that high-level cognition is reflected in high-order dynamic correlations in brain activity
10 patterns. We developed an approach to estimating high-order dynamic correlations in timeseries data, and
11 we applied the approach to neuroimaging data collected as human participants either listened to a ten-
12 minute story, listened to a temporally scrambled version of the story, or underwent a resting state scan. We
13 trained across-participant pattern classifiers to decode (in held-out data) when in the session each neural
14 activity snapshot was collected. We found that classifiers trained to decode from high-order dynamic
15 correlations yielded the best performance on data collected as participants listened to the (unscrambled)
16 story. By contrast, classifiers trained to decode data from scrambled versions of the story or during
17 the resting state scan yielded the best performance when they were trained using first-order dynamic
18 correlations or non-correlational activity patterns. We suggest that as our thoughts become more complex,
19 they are reflected in higher-order patterns of dynamic network interactions throughout the brain.

20 **Introduction**

21 A central goal in cognitive neuroscience is to elucidate the *neural code*: the mapping between (a) mental
22 states or cognitive representations and (b) neural activity patterns. One means of testing models of the
23 neural code is to ask how accurately that model is able to “translate” neural activity patterns into known
24 (or hypothesized) mental states or cognitive representations (e.g., Haxby et al., 2001; Huth et al., 2016, 2012;
25 Kamitani & Tong, 2005; Mitchell et al., 2008; Nishimoto et al., 2011; Norman et al., 2006; Pereira et al.,
26 2018; Tong & Pratte, 2012). Training decoding models on different types of neural features (Fig. 1a) can
27 also help to elucidate which specific aspects of neural activity patterns are informative about cognition—
28 and, by extension, which types of neural activity patterns might comprise the neural code. For example,
29 prior work has used region of interest analyses to estimate the anatomical locations of specific neural
30 representations (e.g., Etzel et al., 2009), or to compare the relative contributions to the neural code of

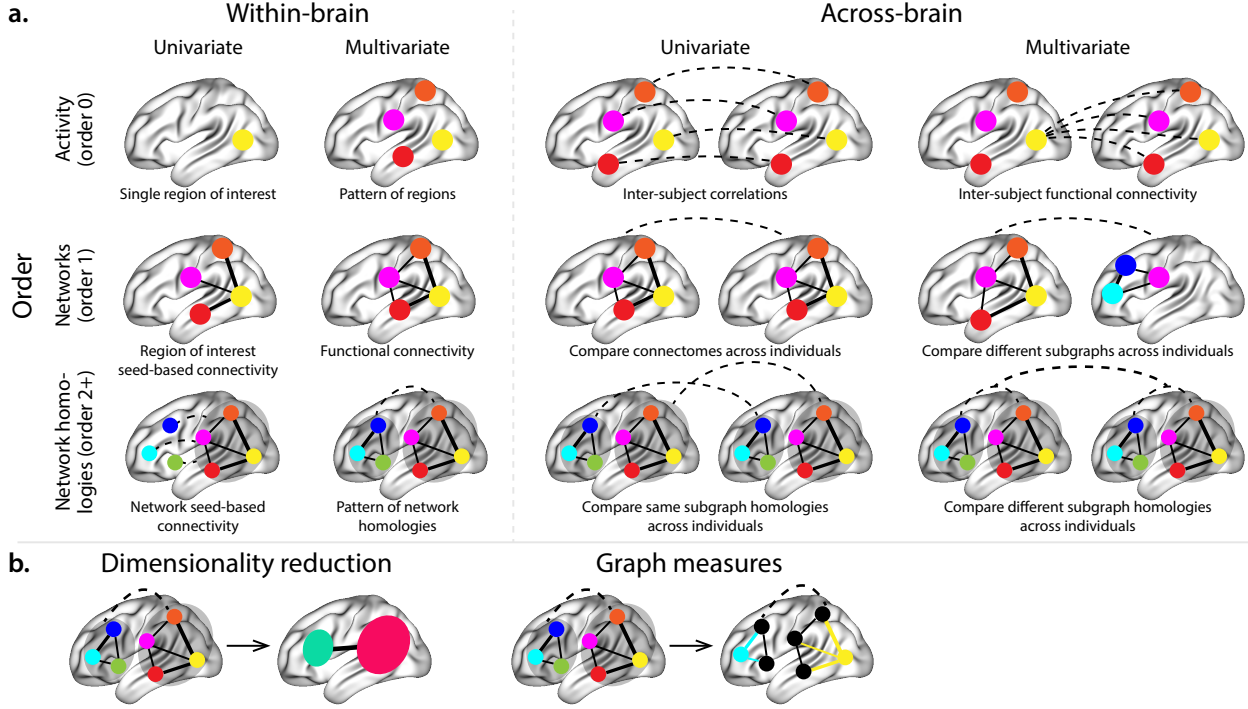


Figure 1: Neural patterns. a. A space of neural features. Within-brain analyses are carried out within a single brain, whereas across-brain analyses compare neural patterns across two or more individuals' brains. Univariate analyses characterize the activities of individual units (e.g., nodes, small networks, hierarchies of networks, etc.), whereas multivariate analyses characterize the patterns of activities across units. Order 0 patterns involve individual nodes; order 1 patterns involve node-node interactions; order 2 (and higher) patterns relate to interactions between homologous networks. Each of these patterns may be static (e.g., averaging over time) or dynamic. **b. Summarizing neural patterns.** To efficiently compute with complex neural patterns, it can be useful to characterize the patterns using summary measures. Dimensionality reduction algorithms project the patterns onto lower-dimensional spaces whose dimensions reflect weighted combinations or non-linear transformations of the dimensions in the original space. Graph measures characterize each unit's participation in its associated network.

multivariate activity patterns versus dynamic correlations between neural activity patterns (e.g., Fong et al., 2019; Manning et al., 2018). An emerging theme in this literature is that cognition is mediated by dynamic interactions between brain structures (Bassett et al., 2006; Demertzi et al., 2019; Lurie et al., 2018; Mack et al., 2017; Preti et al., 2017; Solomon et al., 2019; Sporns & Honey, 2006; Turk-Browne, 2013; Zou et al., 2019). Studies of the neural code to date have primarily focused on univariate or multivariate neural patterns (for review see Norman et al., 2006), or (more recently) on patterns of dynamic first-order correlations (i.e., interactions between pairs of brain structures; Demertzi et al., 2019; Fong et al., 2019; Lurie et al., 2018; Manning et al., 2018; Preti et al., 2017; Zou et al., 2019). We wondered what the future of this line of work might hold. For example, is the neural code mediated by higher-order interactions between brain structures (e.g., see Reimann et al., 2017)? Second-order correlations reflect *homologous* patterns of

41 correlation. In other words, if the dynamic patterns of correlations between two regions, A and B , are similar
42 to those between two other regions, C and D , this would be reflected in the second-order correlations be-
43 tween ($A-B$) and ($C-D$). In this way, second-order correlations identify similarities and differences between
44 subgraphs of the brain’s connectome. Analogously, third-order correlations reflect homologies between
45 second-order correlations— i.e., homologous patterns of homologous interactions between brain regions.
46 More generally, higher-order correlations reflect homologies between patterns of lower-order correlations.
47 We can then ask: which “orders” of interaction are most reflective of high-level cognitive processes?

48 Another central question pertains to the extent to which the neural code is carried by activity patterns
49 that directly reflect ongoing cognition (e.g., following Haxby et al., 2001; Norman et al., 2006), versus the
50 dynamic properties of the network structure itself, independent of specific activity patterns in any given
51 set of regions (e.g., following Bassett et al., 2006). For example, graph measures such as centrality and
52 degree (Bullmore & Sporns, 2009) may be used to estimate how a given brain structure is “communicating”
53 with other structures, independently of the specific neural representations carried by those structures.
54 If one considers a brain region’s position in the network (e.g., its eigenvector centrality) as a dynamic
55 property, one can compare how the positions of different regions are correlated, and/or how those patterns
56 of correlations change over time. We can also compute higher-order patterns in these correlations to
57 characterize homologous subgraphs in the connectome that display similar changes in their constituent
58 brain structures’ interactions with the rest of the brain.

59 To gain insights into the above aspects of the neural code, we developed a computational framework
60 for estimating dynamic high-order correlations in timeseries data. This framework provides an important
61 advance, in that it enables us to examine patterns of higher-order correlations that are computationally
62 intractable to estimate via conventional methods. Given a multivariate timeseries, our framework provides
63 timepoint-by-timepoint estimates of the first-order correlations, second-order correlations, and so on. Our
64 approach combines a kernel-based method for computing dynamic correlations in timeseries data with a di-
65 mensionality reduction step (Fig. 1b) that projects the resulting dynamic correlations into a low-dimensional
66 space. We explored two dimensionality reduction approaches: principle components analysis (PCA; Pear-
67 son, 1901), which preserves an approximately invertible transformation back to the original data (e.g., this
68 follows related approaches taken by Gonzalez-Castillo et al., 2019; McIntosh & Jirsa, 2019; Toker & Som-
69 mer, 2019); and a second non-invertible algorithm that explored patterns in eigenvector centrality (Landau,
70 1895). This latter approach characterizes correlations between each feature dimension’s relative *position* in
71 the network in favor of the specific activity histories of different features (also see Betzel et al., 2019; Reimann
72 et al., 2017; Sizemore et al., 2018).

73 We validated our approach using synthetic data where the underlying correlations were known. We

74 then applied our framework to a neuroimaging dataset collected as participants listened to either an audio
75 recording of a ten-minute story, listened to a temporally scrambled version of the story, or underwent a
76 resting state scan (Simony et al., 2016). We used a subset of the data to train across-participant classifiers
77 to decode listening times using a blend of neural features (comprising neural activity patterns, as well as
78 different orders of dynamic correlations between those patterns that were inferred using our computational
79 framework). We found that both the PCA-based and eigenvector centrality-based approaches yielded neural
80 patterns that could be used to decode accurately (i.e., well above chance). Both approaches also yielded
81 the best decoding accuracy for data collected during (intact) story listening when high-order (PCA: second-
82 order; eigenvector centrality: fourth-order) dynamic correlation patterns were included as features. When
83 we trained classifiers on the scrambled stories or resting state data, only lower-order dynamic patterns were
84 informative to the decoders. Taken together, our results indicate that high-level cognition is supported by
85 high-order dynamic patterns of communication between brain structures.

86 Methods

87 Our general approach to efficiently estimating high-order dynamic correlations comprises four general
88 steps (Fig. 2). First, we derive a kernel-based approach to computing dynamic pairwise correlations in
89 a T (timepoints) by K (features) multivariate timeseries, \mathbf{X}_0 . This yields a T by $O(K^2)$ matrix of dynamic
90 correlations, \mathbf{Y}_1 , where each row comprises the upper triangle and diagonal of the correlation matrix at
91 a single timepoint, reshaped into a row vector (this reshaped vector is $(\frac{K^2-K}{2} + K)$ -dimensional). Second,
92 we apply a dimensionality reduction step to project the matrix of dynamic correlations back onto a K -
93 dimensional space. This yields a T by K matrix, \mathbf{X}_1 , that reflects an approximation of the dynamic correlations
94 reflected in the original data. Third, we use repeated applications of the kernel-based dynamic correlation
95 step to \mathbf{X}_n and the dimensionality reduction step to the resulting \mathbf{Y}_{n+1} to estimate high-order dynamic
96 correlations. Each application of these steps to a T by K time series \mathbf{X}_n yields a T by K matrix, \mathbf{X}_{n+1} , that
97 reflects the dynamic correlations between the columns of \mathbf{X}_n . In this way, we refer to n as the *order* of the
98 timeseries, where \mathbf{X}_0 (order 0) denotes the original data and \mathbf{X}_n denotes (approximated) n^{th} -order dynamic
99 correlations between the columns of \mathbf{X}_0 . Finally, we use a cross-validation-based decoding approach to
100 evaluate how well information contained in a given order (or weighted mixture of orders) may be used
101 to decode relevant cognitive states. If including a given \mathbf{X}_n in the feature set yields higher classification
102 accuracy on held-out data, we interpret this as evidence that the given cognitive states are reflected in
103 patterns of n^{th} -order correlations. All of the code used to produce the figures and results in this manuscript,
104 along with links to the corresponding datasets, may be found at github.com/ContextLab/timecorr-paper. In

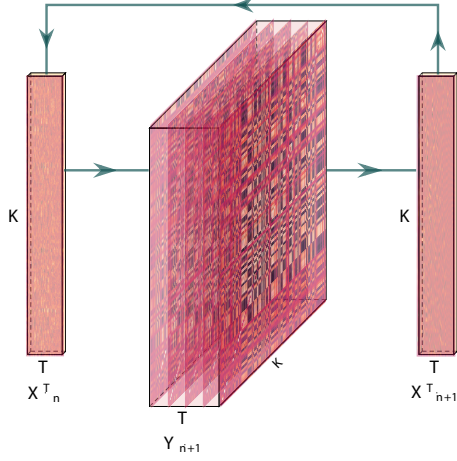


Figure 2: **Estimating dynamic high-order correlations.** Given a T by K matrix of multivariate timeseries data, \mathbf{X}_n (where $n \in \mathbb{N}, n \geq 0$), we use Equation 4 to compute a timeseries of K by K correlation matrices, \mathbf{Y}_{n+1} . We then approximate \mathbf{Y}_{n+1} with the T by K matrix \mathbf{X}_{n+1} . This process may be repeated to scalably estimate iteratively higher-order correlations in the data. Note that the transposes of \mathbf{X}_n and \mathbf{X}_{n+1} are displayed in the figure for compactness.

105 addition, we have released a Python toolbox for computing dynamic high-order correlations in timeseries
 106 data; our toolbox may be found at timecorr.readthedocs.io.

107 Kernel-based approach for computing dynamic correlations

Given a T by K matrix of observations, \mathbf{X} , we can compute the (static) Pearson's correlation between any pair of columns, $\mathbf{X}(\cdot, i)$ and $\mathbf{X}(\cdot, j)$ using (Pearson, 1901):

$$\text{corr}(\mathbf{X}(\cdot, i), \mathbf{X}(\cdot, j)) = \frac{\sum_{t=1}^T (\mathbf{X}(t, i) - \bar{\mathbf{X}}(\cdot, i)) (\mathbf{X}(t, j) - \bar{\mathbf{X}}(\cdot, j))}{\sqrt{\sum_{t=1}^T \sigma_{\mathbf{X}(\cdot, i)}^2 \sigma_{\mathbf{X}(\cdot, j)}^2}}, \text{ where} \quad (1)$$

$$\bar{\mathbf{X}}(\cdot, k) = \frac{1}{T} \sum_{t=1}^T \mathbf{X}(t, k), \text{ and} \quad (2)$$

$$\sigma_{\mathbf{X}(\cdot, k)}^2 = \frac{1}{T} \sum_{t=1}^T (\mathbf{X}(t, k) - \bar{\mathbf{X}}(\cdot, k))^2 \quad (3)$$

108 We can generalize this formula to compute time-varying correlations by incorporating a *kernel function* that
 109 takes a time t as input, and returns how much the observed data at each timepoint $\tau \in [-\infty, \infty]$ contributes
 110 to the estimated instantaneous correlation at time t (Fig. 3; also see Allen et al., 2012, for a similar approach).

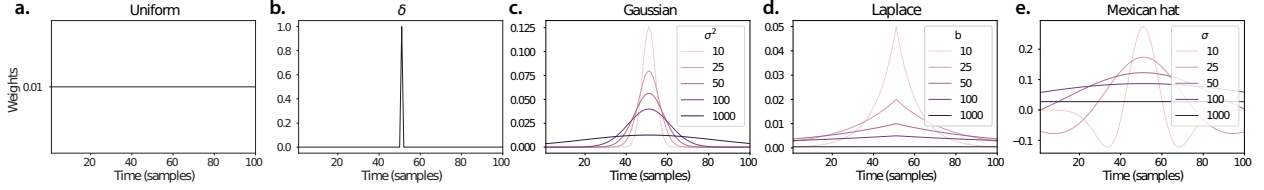


Figure 3: Examples of kernel functions. Each panel displays per-timepoint weights for a kernel centered at $t = 50$, evaluated at 100 timepoints ($\tau \in [1, \dots, 100]$). **a. Uniform kernel.** The weights are timepoint-invariant; observations at all timepoints are weighted equally, and do not change as a function of τ . This is a special case kernel function that reduces dynamic correlations to static correlations. **b. Dirac δ kernel.** Only the observation at timepoint t is given a non-zero weight (of 1). **c. Gaussian kernels.** Each kernel's weights fall off in time according to a Gaussian probability density function centered on time t . Weights derived using several different example width parameters (σ^2) are displayed. **d. Laplace kernels.** Each kernel's weights fall off in time according to a Laplace probability density function centered on time t . Weights derived using several different example width parameters (b) are displayed. **e. Mexican hat (Ricker wavelet) kernels.** Each kernel's weights fall off in time according to a Ricker wavelet centered on time t . This function highlights the *contrasts* between local versus surrounding activity patterns in estimating dynamic correlations. Weights derived using several different example width parameters (σ) are displayed.

Given a kernel function $\kappa_t(\cdot)$ for timepoint t , evaluated at timepoints $\tau \in [1, \dots, T]$, we can update the static correlation formula in Equation 1 to estimate the *instantaneous correlation* at timepoint t :

$$\text{timecorr}_{\kappa_t}(\mathbf{X}(\cdot, i), \mathbf{X}(\cdot, j)) = \frac{\sum_{\tau=1}^T (\mathbf{X}(\tau, i) - \tilde{\mathbf{X}}_{\kappa_t}(\cdot, i))(\mathbf{X}(\tau, j) - \tilde{\mathbf{X}}_{\kappa_t}(\cdot, j))}{\sqrt{\sum_{\tau=1}^T \tilde{\sigma}_{\kappa_t}^2(\mathbf{X}(\cdot, i)) \tilde{\sigma}_{\kappa_t}^2(\mathbf{X}(\cdot, j))}}, \text{ where} \quad (4)$$

$$\tilde{\mathbf{X}}_{\kappa_t}(\cdot, k) = \sum_{\tau=1}^T \kappa_t(\tau) \mathbf{X}(\tau, k), \quad (5)$$

$$\tilde{\sigma}_{\kappa_t}^2(\mathbf{X}(\cdot, k)) = \sum_{\tau=1}^T (\mathbf{X}(\tau, k) - \tilde{\mathbf{X}}_{\kappa_t}(\cdot, k))^2. \quad (6)$$

112 Here $\text{timecorr}_{\kappa_t}(\mathbf{X}(\cdot, i), \mathbf{X}(\cdot, j))$ reflects the correlation at time t between columns i and j of \mathbf{X} , estimated using
 113 the kernel κ_t . We evaluate Equation 4 in turn for each pair of columns in \mathbf{X} and for kernels centered on each
 114 timepoint in the timeseries, respectively, to obtain a T by K by K timeseries of dynamic correlations, \mathbf{Y} . For
 115 convenience, we then reshape the upper triangles and diagonals of each timepoint's correlation matrix into
 116 a row vector to obtain an equivalent T by $(\frac{K^2-K}{2} + K)$ matrix.

117 **Dynamic inter-subject functional connectivity (DISFC)**

Equation 4 provides a means of taking a single observation matrix, \mathbf{X}_n and estimating the dynamic correlations from moment to moment, \mathbf{Y}_{n+1} . Suppose that one has access to a set of multiple observation matrices that reflect the same phenomenon. For example, one might collect neuroimaging data from several experimental participants, as each participant performs the same task (or sequence of tasks). Let $\mathbf{X}_n^1, \mathbf{X}_n^2,$

..., \mathbf{X}_n^P reflect the T by K observation matrices ($n = 0$) or reduced correlation matrices ($n > 0$) for each of P participants in an experiment. We can use *inter-subject functional connectivity* (ISFC; Simony et al., 2016) to compute the stimulus-driven correlations reflected in the multi-participant dataset at a given timepoint t using:

$$\bar{\mathbf{C}}(t) = M \left(R \left(\frac{1}{2P} \sum_{p=1}^P Z(\mathbf{Y}_{n+1}^p(t))^\top + Z(\mathbf{Y}_{n+1}^p(t)) \right) \right), \quad (7)$$

where M extracts and vectorizes the upper triangle and diagonal of a symmetric matrix, Z is the Fisher z-transformation (Zar, 2010):

$$Z(r) = \frac{\log(1+r) - \log(1-r)}{2}, \quad (8)$$

R is the inverse of Z :

$$R(z) = \frac{\exp(2z-1)}{\exp(2z+1)}, \quad (9)$$

and $\mathbf{Y}_{n+1}^p(t)$ denotes the correlation matrix at timepoint t (Eqn. 4) between each column of \mathbf{X}_n^p and each column of the average \mathbf{X}_n from all *other* participants, $\bar{\mathbf{X}}_n^{\setminus p}$:

$$\bar{\mathbf{X}}_n^{\setminus p} = \frac{1}{P-1} \sum_{q \in \setminus p} \mathbf{X}_n^q, \quad (10)$$

118 where $\setminus p$ denotes the set of all participants other than participant p . In this way, the T by $(\frac{K^2-K}{2} + K)$ DISFC
119 matrix $\bar{\mathbf{C}}$ provides a time-varying extension of the ISFC approach developed by Simony et al. (2016).

120 Low-dimensional representations of dynamic correlations

121 Given a T by $(\frac{K^2-K}{2} + K)$ matrix of n^{th} -order dynamic correlations, \mathbf{Y}_n , we propose two general approaches
122 to computing a T by K low-dimensional representation of those correlations, \mathbf{X}_n . The first approach uses
123 dimensionality reduction algorithms to project \mathbf{Y}_n onto a K -dimensional space. The second approach uses
124 graph measures to characterize the relative positions of each feature ($k \in [1, \dots, K]$) in the network defined
125 by the correlation matrix at each timepoint.

126 **Dimensionality reduction-based approaches to computing \mathbf{X}_n**

127 The modern toolkit of dimensionality reduction algorithms include Principal Components Analysis (PCA;
128 Pearson, 1901), Probabilistic PCA (PPCA; Tipping & Bishop, 1999), Exploratory Factor Analysis (EFA;
129 Spearman, 1904), Independent Components Analysis (ICA; Comon et al., 1991; Jutten & Herault, 1991), t -
130 Stochastic Neighbor Embedding (t -SNE; van der Maaten & Hinton, 2008), Uniform Manifold Approximation
131 and Projection (UMAP; McInnes et al., 2018), non-negative matrix factorization (NMF; Lee & Seung, 1999),
132 Topographic Factor Analysis (TFA; Manning et al., 2014), Hierarchical Topographic Factor analysis (HTFA;
133 Manning et al., 2018), Topographic Latent Source Analysis (TLSA; Gershman et al., 2011), dictionary learn-
134 ing (J. Mairal et al., 2009; J. B. Mairal et al., 2009), and deep auto-encoders (Hinton & Salakhutdinov, 2006),
135 among others. While complete characterizations of each of these algorithms is beyond the scope of the
136 present manuscript, the general intuition driving these approaches is to compute the T by K matrix, \mathbf{X} , that
137 is closest to the original T by J matrix, \mathbf{Y} , where (typically) $K \ll J$. The different approaches place different
138 constraints on what properties \mathbf{X} must satisfy and which aspects of the data are compared (and how) in
139 order to optimize how well \mathbf{X} approximates \mathbf{Y} .

140 Applying dimensionality reduction algorithms to \mathbf{Y} yields an \mathbf{X} whose columns reflect weighted combi-
141 nations (or nonlinear transformations) of the original columns of \mathbf{Y} . This has two main consequences. First,
142 with each repeated dimensionality reduction, the resulting \mathbf{X}_n has lower and lower fidelity (with respect to
143 what the “true” \mathbf{Y}_n might have looked like without using dimensionality reduction to maintain scalability).
144 In other words, computing \mathbf{X}_n is a lossy operation. Second, whereas each column of \mathbf{Y}_n may be mapped
145 directly onto specific pairs of columns of \mathbf{X}_{n-1} , the columns of \mathbf{X}_n reflect weighted combinations and/or
146 nonlinear transformations of the columns of \mathbf{Y}_n . Many dimensionality reduction algorithms are invertible
147 (or approximately invertible). However, attempting to map a given \mathbf{X}_n back onto the original feature space
148 of \mathbf{X}_0 will usually require $O(TK^{2n})$ space and therefore becomes intractable as n or K grow large.

149 **Graph measure approaches to computing \mathbf{X}_n**

150 The above dimensionality reduction approaches to approximating a given \mathbf{Y}_n with a lower-dimensional
151 \mathbf{X}_n preserve a (potentially recombined and transformed) mapping back to the original data in \mathbf{X}_0 . We also
152 explore graph measures that instead characterize each feature’s relative *position* in the broader network of
153 interactions and connections. To illustrate the distinction between the two general approaches we explore,
154 suppose a network comprises nodes A , B , and C . If A and B exhibit uncorrelated activity patterns, the
155 functional connection (correlation) between them will be (by definition) close to 0. However, if A and B
156 each interact with C in similar ways, we might attempt to capture those similarities using a measure that

157 reflects how A and B interact with *other* members of the network.

158 In general, graph measures take as input a matrix of interactions (e.g., using the above notation, a K
159 by K correlation matrix or binarized correlation matrix reconstituted from a single timepoint's row of \mathbf{Y}),
160 and return as output a set of K measures describing how each node (feature) sits within that correlation
161 matrix with respect to the rest of the population. Widely used measures include betweenness centrality (the
162 proportion of shortest paths between each pair of nodes in the population that involves the given node
163 in question; e.g., Barthélemy, 2004; Freeman, 1977; Geisberger et al., 2008; Newman, 2005; Opsahl et al.,
164 2010); diversity and dissimilarity (characterizations of how differently connected a given node is from others
165 in the population; e.g., Lin, 2009; Rao, 1982; Ricotta & Szeidl, 2006); eigenvector centrality and pagerank
166 centrality (measures of how influential a given node is within the broader network; e.g., Bonacich, 2007;
167 Halu et al., 2013; Lohmann et al., 2010; Newman, 2008); transfer entropy and flow coefficients (a measure of
168 how much information is flowing from a given node to other nodes in the network; e.g., Honey et al., 2007;
169 Schreiber, 2000); k -coreness centrality (a measure of the connectivity of a node within its local subgraph; e.g.,
170 Alvarez-Hamelin et al., 2005; Christakis & Fowler, 2010); within-module degree (a measure of how many
171 connections a node has to its close neighbors in the network; e.g., Rubinov & Sporns, 2010); participation
172 coefficient (a measure of the diversity of a node's connections to different subgraphs in the network; e.g.,
173 Rubinov & Sporns, 2010); and subgraph centrality (a measure of a node's participation in all of the network's
174 subgraphs; e.g., Estrada & Rodríguez-Velázquez, 2005); among others.

175 For a given graph measure, $\eta : \mathbb{R}^{K \times K} \rightarrow \mathbb{R}^K$, we can use η to transform each row of \mathbf{Y}_n in a way that
176 characterizes the corresponding graph properties of each column. This results in a new T by K matrix,
177 \mathbf{X}_n , that reflects how the features reflected in the columns of \mathbf{X}_{n-1} participate in the network during each
178 timepoint (row).

179 Dynamic higher-order correlations

180 Because \mathbf{X}_n has the same shape as the original data \mathbf{X}_0 , approximating \mathbf{Y}_n with a lower-dimensional \mathbf{X}_n
181 enables us to estimate high-order dynamic correlations in a scalable way. Given a T by K input matrix, the
182 output of Equation 4 requires $O(TK^2)$ space to store. Repeated applications of Equation 4 (i.e., computing
183 dynamic correlations between the columns of the outputted dynamic correlation matrix) each require
184 exponentially more space; in general the n^{th} -order dynamic correlations of a T by K timeseries occupies
185 $O(TK^{2n})$ space. However, when we approximate or summarize the output of Equation 4 with a T by K matrix
186 (as described above), it becomes feasible to compute even very high-order correlations in high-dimensional
187 data. Specifically, approximating the n^{th} -order dynamic correlations of a T by K timeseries requires only

188 $O(TK^2)$ additional space– the same as would be required to compute first-order dynamic correlations. In
189 other words, the space required to store $n + 1$ multivariate timeseries reflecting up to n^{th} order correlations
190 in the original data scales linearly with n using our approach (Fig. 2).

191 Data

192 We examined two types of data: synthetic data and human functional neuroimaging data. We constructed
193 and leveraged the synthetic data to evaluate our general approach (for a related validation approach see
194 Thompson et al., 2018). Specifically, we tested how well Equation 4 could be used to recover known dynamic
195 correlations using different choices of kernel (κ ; Fig. 3), for each of several synthetic datasets that exhibited
196 different temporal properties. We also used this synthetic data to simulate higher-order correlations and
197 tested how well Equation 4 could recover these correlations using the best kernel from the previous synthetic
198 data analysis. We applied our approach to a functional neuroimaging dataset to test the hypothesis that
199 ongoing cognitive processing is reflected in high-order dynamic correlations. We used an across-participant
200 classification test to estimate whether dynamic correlations of different orders contain information about
201 which timepoint in a story participants were listening to.

202 Synthetic data

203 We constructed a total of 40 different multivariate timeseries, collectively reflecting a total of 4 qualitatively
204 different patterns of dynamic correlations (i.e., 10 datasets reflecting each type of dynamic pattern). Each
205 timeseries comprised 50 features (dimensions) that varied over 300 timepoints. The observations at each
206 timepoint were drawn from a zero-mean multivariate Gaussian distribution with a covariance matrix
207 defined for each timepoint as described below. We drew the observations at each timepoint independently
208 from the draws at all other timepoints; in other words, for each observation $s_t \sim \mathcal{N}(\mathbf{0}, \Sigma_t)$ at timepoint t ,
209 $p(s_t) = p(s_t | s_{\setminus t})$.

Constant. We generated data with stable underlying correlations to evaluate how Equation 4 characterized correlation “dynamics” when the ground truth correlations were static. We constructed 10 multivariate timeseries whose observations were each drawn from a single (stable) Gaussian distribution. For each dataset (indexed by m), we constructed a random covariance matrix, Σ_m :

$$\mathbf{C}(i, j) \sim \mathcal{N}(0, 1) \tag{11}$$

$$\Sigma_m = \mathbf{C}\mathbf{C}^\top, \text{ where} \tag{12}$$

210 $i, j \in [1, 2, \dots, 50]$. In other words, all of the observations (for each of the 300 timepoints) within each dataset
 211 were drawn from a multivariate Gaussian distribution with the same covariance matrix, and the 10 datasets
 212 each used a different covariance matrix.

213 **Random.** We generated a second set of 10 synthetic datasets whose observations at each timepoint were
 214 drawn from a Gaussian distribution with a new randomly constructed (using Eqn. 12) covariance matrix.
 215 Because each timepoint's covariance matrix was drawn independently from the covariance matrices for all
 216 other timepoints, these datasets provided a test of reconstruction accuracy in the absence of any meaningful
 217 underlying temporal structure in the dynamic correlations underlying the data.

Ramping. We generated a third set of 10 synthetic datasets whose underlying correlations changed gradually over time. For each dataset, we constructed two *anchor* covariance matrices using Equation 12, Σ_{start} and Σ_{end} . For each of the 300 timepoints in each dataset, we drew the observations from a multivariate Gaussian distribution whose covariance matrix at each timepoint $t \in [0, \dots, 299]$ was given by

$$\Sigma_t = \left(1 - \frac{t}{299}\right)\Sigma_{\text{start}} + \frac{t}{299}\Sigma_{\text{end}}. \quad (13)$$

218 The gradually changing correlations underlying these datasets allow us to evaluate the recovery of dynamic
 219 correlations when each timepoint's correlation matrix is unique (as in the random datasets), but where the
 220 correlation dynamics are structured and exhibit first-order autocorrelations (as in the constant datasets).

221 **Event.** We generated a fourth set of 10 synthetic datasets whose underlying correlation matrices exhibited
 222 prolonged intervals of stability, interspersed with abrupt changes. For each dataset, we used Equation 12
 223 to generate 5 random covariance matrices. We constructed a timeseries where each set of 60 consecutive
 224 samples was drawn from a Gaussian with the same covariance matrix. These datasets were intended to
 225 simulate a system that undergoes occasional abrupt state changes.

226 Synthetic data: simulating dynamic high-order correlations

227 We developed an iterative procedure for constructing timeseries data that exhibits known dynamic high-
 228 order correlations. The procedure builds on our approach to generating dynamic first-order correlations.
 229 Essentially, once we generate a timeseries with known first-order correlations, we can use the known first-
 230 order correlations as a template to generate a new timeseries of second-order correlations. In turn, we can
 231 generate a timeseries of third-order correlations from the second-order correlations, and so on. In general,
 232 we can generate order n correlations given a timeseries of order $n - 1$ correlations, for any $n > 1$. Finally,

233 given the order n timeseries, we can reverse the preceding process to generate an order $n - 1$ timeseries, an
234 order $n - 2$ order timeseries, and so on, until we obtain an order 0 timeseries of simulated data that reflects
235 the chosen high-order dynamics.

The central mathematical operations in our procedure are two functions, $\text{vec}(\cdot)$ and $\text{mat}(\cdot)$. The $\text{vec}(\cdot)$ function takes as input a $K \times K$ symmetric matrix and returns as output a $(\frac{K^2-K}{2} + K)$ -dimensional column vector containing the entries in the upper triangle and diagonal. The $\text{mat}(\cdot)$ function inverts $\text{vec}(\cdot)$ by taking as input a $(\frac{K^2-K}{2} + K)$ -dimensional column vector and returning a $K \times K$ symmetric matrix as output. We can then generate an order n correlation matrix (for one timepoint, t) from an order $n - 1$ template (from the same timepoint) as follows:

$$\Sigma_n(t) = \text{mat}(\text{vec}(\Sigma_{n-1}(t)) \otimes \text{vec}(\Sigma_{n-1}(t))^\top). \quad (14)$$

Given a timeseries of order n correlation matrices, we can draw an order $n - 1$ correlation matrix for each timepoint t using

$$\sigma_{n-1}(t) \sim \mathcal{N}(\mathbf{0}, \Sigma_n(t)) \quad (15)$$

$$\Sigma_{n-1}(t) = \text{mat}(\sigma_{n-1}(t)). \quad (16)$$

236 We can then use repeated applications of Equations 15 and 16 in order to obtain a synthetic dataset.

237 When the template first-order correlations are constructed to exhibit different temporal profiles (e.g.,
238 using the constant, random, ramping, and event procedures described above), the resulting high-order
239 correlations and synthetic data will exhibit the same category of temporal profile.

240 Following our approach to generating synthetic data exhibiting known first-order correlations, we
241 constructed a total of 40 additional multivariate timeseries, collectively reflecting a total of 4 qualitatively
242 different patterns of dynamic correlations (i.e., 10 datasets reflecting each type of dynamic pattern: constant,
243 random, ramping, and event).

244 **Functional neuroimaging data collected during story listening**

245 We examined an fMRI dataset collected by Simony et al. (2016) that the authors have made publicly available
246 at arks.princeton.edu/ark:/88435/dsp015d86p269k. The dataset comprises neuroimaging data collected as
247 participants listened to an audio recording of a story (intact condition; 36 participants), listened to temporally
248 scrambled recordings of the same story (17 participants in the paragraph-scrambled condition listened to
249 the paragraphs in a randomized order and 36 in the word-scrambled condition listened to the words in a

250 randomized order), or lay resting with their eyes open in the scanner (rest condition; 36 participants). Full
251 neuroimaging details may be found in the original paper for which the data were collected (Simony et al.,
252 2016).

253 **Hierarchical topographic factor analysis (HTFA).** Following our prior related work, we used HTFA (Manning et al., 2018) to derive a compact representation of the neuroimaging data. In brief, this approach approximates the timeseries of voxel activations (44,415 voxels) using a much smaller number of radial basis function (RBF) nodes (in this case, 700 nodes, as determined by an optimization procedure described by Manning et al., 2018). This provides a convenient representation for examining full-brain network dynamics.
254 All of the analyses we carried out on the neuroimaging dataset were performed in this lower-dimensional
255 space. In other words, each participant’s data matrix, X_0 , was a number-of-timepoints by 700 matrix of
256 HTFA-derived factor weights (where the row and column labels were matched across participants). Code
257 for carrying out HTFA on fMRI data may be found as part of the BrainIAK toolbox (Capota et al., 2017),
258 which may be downloaded at brainiak.org.
259

263 **Temporal decoding**

264 We sought to identify neural patterns that reflected participants’ ongoing cognitive processing of incoming
265 stimulus information. As reviewed by Simony et al. (2016), one way of homing in on these stimulus-
266 driven neural patterns is to compare activity patterns across individuals (e.g., using ISFC analyses). In
267 particular, neural patterns will be similar across individuals to the extent that the neural patterns under
268 consideration are stimulus-driven, and to the extent that the corresponding cognitive representations are
269 reflected in similar spatial patterns across people. Following this logic, we used an across-participant
270 temporal decoding test developed by Manning et al. (2018) to assess the degree to which different neural
271 patterns reflected ongoing stimulus-driven cognitive processing across people. The approach entails using
272 a subset of the data to train a classifier to decode stimulus timepoints (i.e., moments in the story participants
273 listened to) from neural patterns. We use decoding (forward inference) accuracy on held-out data, from held-
274 out participants, as a proxy for the extent to which the inputted neural patterns reflected stimulus-driven
275 cognitive processing in a similar way across individuals.

276 **Forward inference and decoding accuracy**

277 We used an across-participant correlation-based classifier to decode which stimulus timepoint matched
278 each timepoint’s neural pattern. We first divided the participants into two groups: a template group,

279 $\mathcal{G}_{\text{template}}$, and a to-be-decoded group, $\mathcal{G}_{\text{decode}}$. We used Equation 7 to compute a DISFC matrix for each
280 group ($\bar{\mathbf{C}}_{\text{template}}$ and $\bar{\mathbf{C}}_{\text{decode}}$, respectively). We then correlated the rows of $\bar{\mathbf{C}}_{\text{template}}$ and $\bar{\mathbf{C}}_{\text{decode}}$ to form a
281 number-of-timepoints by number-of-timepoints decoding matrix, Λ . In this way, the rows of Λ reflected
282 timepoints from the template group, while the columns reflected timepoints from the to-be-decoded group.
283 We used Λ to assign temporal labels to each row $\bar{\mathbf{C}}_{\text{decode}}$ using the row of $\bar{\mathbf{C}}_{\text{template}}$ with which it was most
284 highly correlated. We then repeated this decoding procedure, but using $\mathcal{G}_{\text{decode}}$ as the template group
285 and $\mathcal{G}_{\text{template}}$ as the to-be-decoded group. Given the true timepoint labels (for each group), we defined the
286 *decoding accuracy* as the average proportion of correctly decoded timepoints, across both groups. We defined
287 the *relative decoding accuracy* as the difference between the decoding accuracy and chance accuracy (i.e., $\frac{1}{T}$).

288 Feature weighting and testing

289 We sought to examine which types of neural features (i.e., activations, first-order dynamic correlations, and
290 higher-order dynamic correlations) were informative to the temporal decoders. Using the notation above,
291 these features correspond to $\mathbf{X}_0, \mathbf{X}_1, \mathbf{X}_2, \mathbf{X}_3$, and so on.

292 One challenge to fairly evaluating high-order correlations is that if the kernel used in Equation 4 is
293 wider than a single timepoint, each repeated application of the equation will result in further temporal
294 blur. Because our primary assessment metric is temporal decoding accuracy, this unfairly biases against
295 detecting meaningful signal in higher-order correlations (relative to lower-order correlations). We attempted
296 to mitigate temporal blur in estimating each \mathbf{X}_n by using a Dirac δ function kernel (which places all of its
297 mass over a single timepoint; Fig. 3b) to compute each lower-order correlation ($\mathbf{X}_1, \mathbf{X}_2, \dots, \mathbf{X}_{n-1}$). We then
298 used a new (potentially wider, as described below) kernel to compute \mathbf{X}_n from \mathbf{X}_{n-1} . In this way, temporal
299 blurring was applied only in the last step of computing \mathbf{X}_n . We note that, because each \mathbf{X}_n is a low-
300 dimensional representation of the corresponding \mathbf{Y}_n , the higher-order correlations we estimated reflect true
301 correlations in the data with lower-fidelity than estimates of lower-order correlations. Therefore, even
302 after correcting for temporal blurring, our approach is still biased against finding meaningful signal in
303 higher-order correlations.

304 After computing each $\mathbf{X}_1, \mathbf{X}_2, \dots, \mathbf{X}_{n-1}$ for each participant, we divided participants into two equally sized
305 groups (± 1 for odd numbers of participants): $\mathcal{G}_{\text{train}}$ and $\mathcal{G}_{\text{test}}$. We then further subdivided $\mathcal{G}_{\text{train}}$ into $\mathcal{G}_{\text{train}_1}$
306 and $\mathcal{G}_{\text{train}_2}$. We then computed Λ (temporal correlation) matrices for each type of neural feature, using $\mathcal{G}_{\text{train}_1}$
307 and $\mathcal{G}_{\text{train}_2}$. This resulted in $n + 1$ Λ matrices (one for the original timeseries of neural activations, and one
308 for each of n orders of dynamic correlations). Our objective was to find a set of weights for each of these
309 Λ matrices such that the weighted average of the $n + 1$ matrices yielded the highest decoding accuracy.

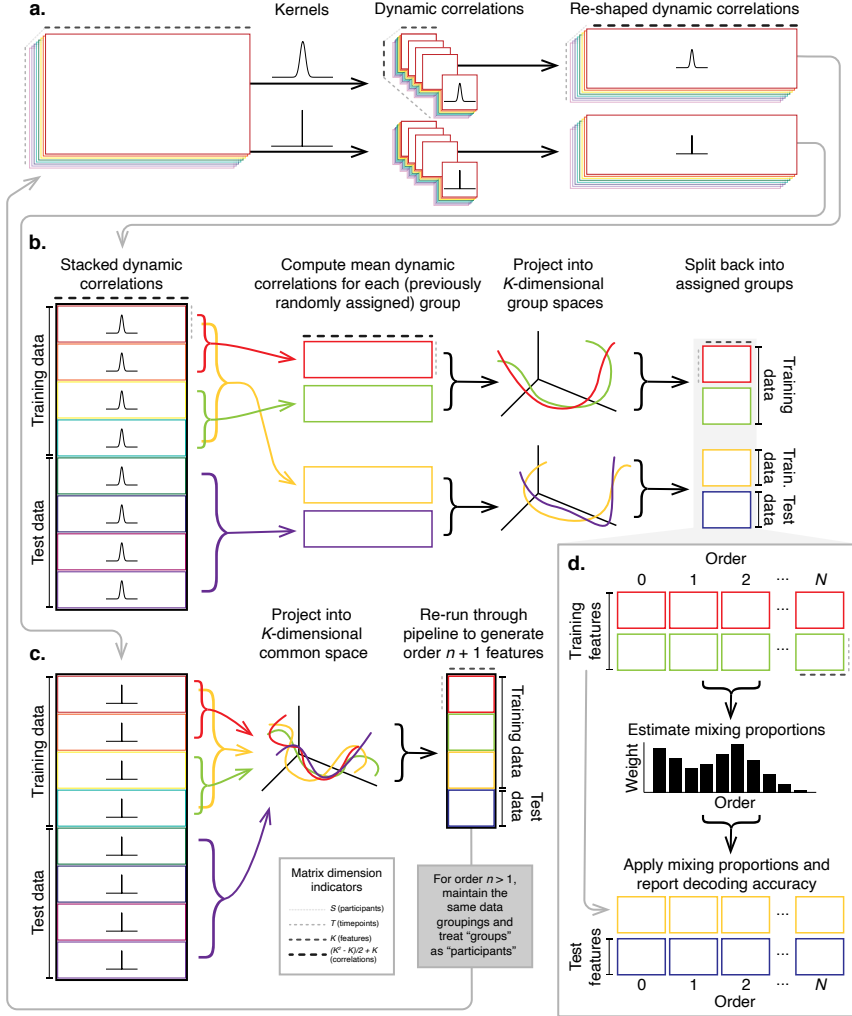


Figure 4: Across-participant timepoint decoding accuracy varies with correlation order and cognitive engagement. **a. Decoding accuracy as a function of order: PCA.** Order (x -axis) refers to the maximum order of dynamic correlations that were available to the classifiers (see *Feature weighting and testing*). The reported across-participant decoding accuracies are averaged over all kernel shapes and widths (see *Identifying robust decoding results*). The y -values are displayed relative to chance accuracy (intact: $\frac{1}{300}$; paragraph: $\frac{1}{272}$; word: $\frac{1}{300}$; rest: $\frac{1}{400}$). The error ribbons denote 95% confidence intervals across cross-validation folds (i.e., random assignments of participants to the training and test sets). The colors denote the experimental condition. Arrows denote sets of features that yielded reliably higher (upwards facing) or lower (downward facing) decoding accuracy than the mean of all other features (via a two-tailed test, thresholded at $p < 0.05$). Figure 8 displays additional comparisons between the decoding accuracies achieved using different sets of neural features. The circled values represent the maximum decoding accuracy within each experimental condition. **b. Normalized timepoint decoding accuracy as a function of order: PCA.** This panel displays the same results as Panel a, but here each curve has been normalized to have a maximum value of 1 and a minimum value of 0 (including the upper and lower bounds of the respective 95% confidence intervals). Panels a and b used PCA to project each high-dimensional pattern of dynamic correlations onto a lower-dimensional space. **c. Timepoint decoding accuracy as a function of order: eigenvector centrality.** This panel is in the same format as Panel a, but here eigenvector centrality has been used to project the high-dimensional patterns of dynamic correlations onto a lower-dimensional space. **d. Normalized timepoint decoding accuracy as a function of order: eigenvector centrality.** This panel is in the same format as Panel b, but here eigenvector centrality has been used to project the high-dimensional patterns of dynamic correlations onto a lower-dimensional space.

310 We used quasi-Newton gradient ascent (Nocedal & Wright, 2006), using decoding accuracy (for $\mathcal{G}_{\text{train}_1}$ and
311 $\mathcal{G}_{\text{train}_2}$) as the objective function to be maximized, to find an optimal set of training data-derived weights,
312 $\phi_{0,1,\dots,n}$, where $\sum_{i=0}^n \phi_i = 1$ and where $\phi_i \geq 0 \forall i \in [0, 1, \dots, n]$.

313 After estimating an optimal set of weights, we computed a new set of $n + 1$ Λ matrices correlating the
314 DISFC patterns from $\mathcal{G}_{\text{train}}$ and $\mathcal{G}_{\text{test}}$ at each timepoint. We use the resulting decoding accuracy of $\mathcal{G}_{\text{test}}$
315 timepoints (using the weights in $\phi_{0,1,\dots,n}$ to average the Λ matrices) to estimate how informative the set of
316 neural features containing up to n^{th} order correlations were.

317 We used a permutation-based procedure to form stable estimates of decoding accuracy for each set of
318 neural features. In particular, we computed the decoding accuracy for each of 10 random group assignments
319 of $\mathcal{G}_{\text{train}}$ and $\mathcal{G}_{\text{test}}$. We report the mean accuracy (along with 95% confidence intervals) for each set of neural
320 features.

321 **Identifying robust decoding results**

322 The temporal decoding procedure we use to estimate which neural features support ongoing cognitive
323 processing is governed by several parameters. In particular, Equation 4 requires defining a kernel function,
324 which can take on different shapes and widths. For a fixed set of neural features, each of these parameters
325 can yield different decoding accuracies. Further, the best decoding accuracy for a given timepoint may be
326 reliably achieved by one set of parameters, whereas the best decoding accuracy for another timepoint might
327 be reliably achieved by a different set of parameters, and the best decoding accuracy across *all* timepoints
328 might be reliably achieved by still another different set of parameters. Rather than attempting to maximize
329 decoding accuracy, we sought to discover the trends in the data that were robust to classifier parameters
330 choices. Specifically, we sought to characterize how decoding accuracy varied (under different experimental
331 conditions) as a function of which neural features were considered.

332 To identify decoding results that were robust to specific classifier parameter choices, we repeated our
333 decoding analyses after substituting into Equation 4 each of a variety of kernel shapes and widths. We
334 examined Gaussian (Fig. 3c), Laplace (Fig. 3d), and Mexican Hat (Fig. 3e) kernels, each with widths of 5, 10,
335 20, and 50 samples. We then report the average decoding accuracies across all of these parameter choices.
336 This enabled us to (partially) factor out performance characteristics that were parameter-dependent, within
337 the set of parameters we examined.

338 **Reverse inference**

339 The dynamic patterns we examined comprise high-dimensional correlation patterns at each timepoint. To
340 help interpret the resulting patterns in the context of other studies, we created summary maps by computing
341 the across-timepoint average pairwise correlations at each order of analysis (first order, second order, etc.).
342 We selected the 10 strongest (absolute value) correlations at each order. Each correlation is between the
343 dynamic activity patterns (or patterns of dynamic high-order correlations) measured at two RBF nodes
344 (see *Hierarchical Topographic Factor Analysis*). Therefore, the 10 strongest correlations involved up to 20 RBF
345 nodes. Each RBF defines a spatial function whose activations range from 0 to 1. We constructed a map
346 of RBF components that denoted the endpoints of the 10 strongest correlations (we set each RBF to have a
347 maximum value of 1). We then carried out a meta analysis using Neurosynth (Rubin et al., 2017) to identify
348 the 10 terms most commonly associated with the given map. This resulted in a set of 10 terms associated
349 with the average dynamic correlation patterns at each order.

350 **Results**

351 We sought to understand whether high-level cognition is reflected in dynamic patterns of high-order
352 correlations. To that end, we developed a computational framework for estimating the dynamics of stimulus-
353 driven high-order correlations in multivariate timeseries data (see *Dynamic inter-subject functional connectivity*
354 (*DISFC*) and *Dynamic higher-order correlations*). We evaluated the efficacy of this framework at recovering
355 known patterns in several synthetic datasets (see *Synthetic data*). We then applied the framework to a public
356 fMRI dataset collected as participants listened to an auditorily presented story, listened to a temporally
357 scrambled version of the story, or underwent a resting state scan (see *Functional neuroimaging data collected*
358 *during story listening*). We used the relative decoding accuracies of classifiers trained on different sets of
359 neural features to estimate which types of features reflected ongoing cognitive processing.

360 **Recovering known dynamic correlations from synthetic data**

361 We generated synthetic datasets that differed in how the underlying correlations changed over time. For
362 each dataset, we applied Equation 4 with a variety of kernel shapes and widths. We assessed how well
363 the true underlying correlations at each timepoint matched the recovered correlations (Fig. 5). For every
364 kernel and dataset we tested, our approach recovered the correlation dynamics we embedded into the data.
365 However, the quality of these recoveries varied across different synthetic datasets in a kernel-dependent
366 way.

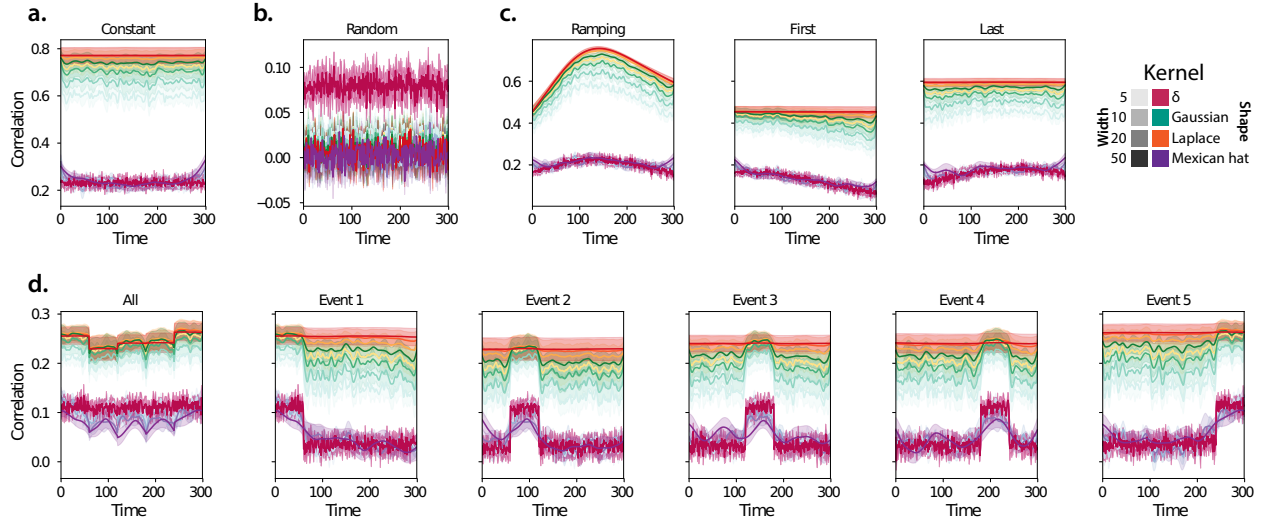


Figure 5: Recovering known dynamic correlations from synthetic data. Each panel displays the average correlations between the vectorized upper triangles of the recovered correlation matrix at each timepoint and either the true underlying correlation at each timepoint or a reference correlation matrix. (The averages are taken across 10 different randomly generated synthetic datasets of the given category.) Error ribbons denote 95% confidence intervals (taken across datasets). Different colors denote different kernel shapes, and the shading within each color family denotes the kernel width parameter. For a complete description of each synthetic dataset, see *Synthetic data*. **a. Constant correlations.** These datasets have a stable (unchanging) underlying correlation matrix. **b. Random correlations.** These datasets are generated using a new independently drawn correlation matrix at each new timepoint. **c. Ramping correlations.** These datasets are generated by smoothly varying the underlying correlations between the randomly drawn correlation matrices at the first and last timepoints. The left panel displays the correlations between the recovered dynamic correlations and the underlying ground truth correlations. The middle panel compares the recovered correlations with the *first* timepoint’s correlation matrix. The right panel compares the recovered correlations with the *last* timepoint’s correlation matrix. **d. Event-based correlations.** These datasets are each generated using five randomly drawn correlation matrices that each remain stable for a fifth of the total timecourse. The left panel displays the correlations between the recovered dynamic correlations and the underlying ground truth correlations. The right panels compare the recovered correlations with the correlation matrices unique to each event.

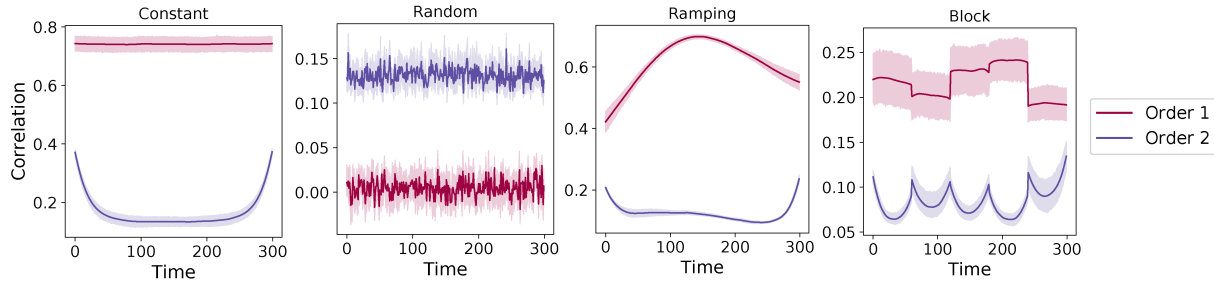


Figure 6: **Recovery of simulated first and second order dynamic correlations.** Each panel displays the average correlations between the vectorized upper triangles of the recovered correlation matrix and the simulated correlation matrix at each timepoint and for each synthetic dataset. (The averages are taken across 10 different randomly generated synthetic datasets of the given category.) Error ribbons denote 95% confidence intervals (taken across datasets). For a complete description of each synthetic dataset, see *Synthetic data*. **a. Constant correlations.** These first and second order dynamic correlation were simulated from datasets have a stable (unchanging) underlying correlation matrix. **b. Random correlations.** These first and second order dynamic correlation were simulated from datasets are generated using a new independently drawn correlation matrix at each new timepoint. **c. Ramping correlations.** These first and second order dynamic correlation were simulated from datasets are generated by smoothly varying the underlying correlations between the randomly drawn correlation matrices at the first and last timepoints and displays the correlations between the recovered dynamic correlations and the simulated correlation first and second order correlation matrices. **d. Event-based correlations.** These first and second order dynamic correlation were simulated from datasets are each generated using five randomly drawn correlation matrices that each remain stable for a fifth of the total timecourse.

367 In general, wide monotonic kernel shapes (Laplace, Gaussian), and wider kernels (within a shape),
 368 performed best when the correlations varied gradually from moment-to-moment (Figs. 5a, c, and d). In the
 369 extreme, as the rate of change in correlations approaches 0 (Fig. 5a), an infinitely wide kernel would exactly
 370 recover the Pearson’s correlation (e.g., compare Eqns. 1 and 4).

371 When the correlation dynamics were unstructured in time (Fig. 5b), a Dirac δ kernel (infinitely narrow)
 372 performed best. This is because, when every timepoint’s correlations are independent of the correlations at
 373 every other timepoint, averaging data over time dilutes the available signal. Following a similar pattern,
 374 holding kernel shape fixed, narrower kernel parameters better recovered randomly varying correlations.

375 Recovering known higher-order dynamic correlations from synthetic data

376 We generated a synthetic timeseries from simulated first and second order dynamic correlation matrices that
 377 differed in how the underlying correlations changed over time. For each dataset, we applied Equation 4 with
 378 a Laplace kernel with a width of 20. We assessed how well the recovered correlations matched simulated
 379 first and second order correlations. (Fig. 6). For every dataset we tested, our approach recovered the
 380 correlation dynamics we embedded into the data. However, the quality of these recoveries varied across
 381 different synthetic datasets.

382 **Cognitively relevant dynamic high-order correlations in fMRI data**

383 We used across-participant temporal decoders to identify cognitively relevant neural patterns in fMRI data
384 (see *Forward inference and decoding accuracy*). The dataset we examined (collected by Simony et al., 2016)
385 comprised four experimental conditions that exposed participants to stimuli that varied systematically in
386 how cognitively engaging they were. The *intact* experimental condition had participants listen to an audio
387 recording of a 10-minute story. The *paragraph*-scrambled experimental condition had participants listen to a
388 temporally scrambled version of the story, where the paragraphs occurred out of order (but where the same
389 total set of paragraphs were presented over the full listening interval). All participants in this condition
390 experienced the scrambled paragraphs in the same order. The *word*-scrambled experimental condition had
391 participants listen to a temporally scrambled version of the story where the words in the story occurred in a
392 random order. All participants in the word condition experienced the scrambled words in the same order.
393 Finally, in a *rest* experimental condition, participants lay in the scanner with no overt stimulus, with their
394 eyes open (blinking as needed). This dataset provided a convenient means of testing our hypothesis that
395 different levels of cognitive processing and engagement are reflected in different orders of brain activity
396 dynamics.

397 In brief, we computed timeseries of dynamic high-order correlations that were similar across participants
398 in each of two randomly assigned groups: a training group and a test group. We then trained classifiers
399 on the training group's data to match each sample from the test group with a stimulus timepoint. Each
400 classifier comprised a weighted blend of neural patterns that reflected up to n^{th} -order dynamic correlations
401 (see *Feature weighting and testing*). We repeated this process for $n \in \{0, 1, 2, \dots, 10\}$. Our examinations of
402 synthetic data suggested that none of the kernels we examined were "universal" in the sense of optimally
403 recovering underlying correlations regardless of the temporal structure of those correlations. We found a
404 similar pattern in the (real) fMRI data, whereby different kernels yielded different decoding accuracies, but
405 no single kernel emerged as the clear "best." In our analyses of neural data, we therefore averaged our
406 decoding results over a variety of kernel shapes and widths in order to identify results that were robust to
407 specific kernel parameters (see *Identifying robust decoding results*).

408 Our approach to estimating dynamic high-order correlations entails mapping the high-dimensional
409 feature space of correlations (a T by $O(K^2)$ matrix) onto a lower-dimensional T by K matrix. We carried out
410 two sets of analyses that differed in how this mapping was computed. The first set of analyses used PCA
411 to find a low-dimensional embedding of the original dynamic correlation matrices (Fig. 7a,b). The second
412 set of analyses characterized correlations in dynamics of each feature's eigenvector centrality, but did not
413 preserve the underlying activity dynamics (Fig. 7c,d).

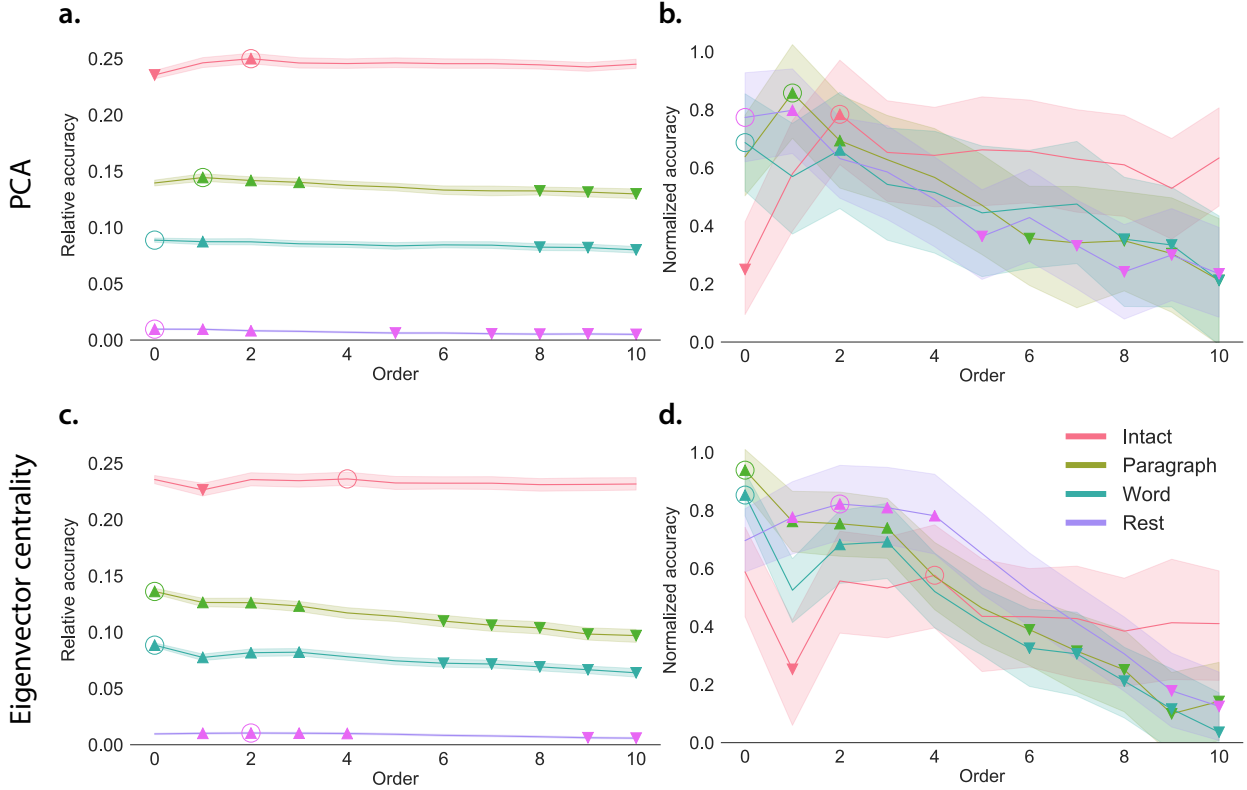


Figure 7: Across-participant timepoint decoding accuracy varies with correlation order and cognitive engagement. **a. Decoding accuracy as a function of order: PCA.** Order (*x*-axis) refers to the maximum order of dynamic correlations that were available to the classifiers (see *Feature weighting and testing*). The reported across-participant decoding accuracies are averaged over all kernel shapes and widths (see *Identifying robust decoding results*). The *y*-values are displayed relative to chance accuracy (intact: $\frac{1}{300}$; paragraph: $\frac{1}{272}$; word: $\frac{1}{300}$; rest: $\frac{1}{400}$). The error ribbons denote 95% confidence intervals across cross-validation folds (i.e., random assignments of participants to the training and test sets). The colors denote the experimental condition. Arrows denote sets of features that yielded reliably higher (upwards facing) or lower (downward facing) decoding accuracy than the mean of all other features (via a two-tailed test, thresholded at $p < 0.05$). Figure 8 displays additional comparisons between the decoding accuracies achieved using different sets of neural features. The circled values represent the maximum decoding accuracy within each experimental condition. **b. Normalized timepoint decoding accuracy as a function of order: PCA.** This panel displays the same results as Panel a, but here each curve has been normalized to have a maximum value of 1 and a minimum value of 0 (including the upper and lower bounds of the respective 95% confidence intervals). Panels a and b used PCA to project each high-dimensional pattern of dynamic correlations onto a lower-dimensional space. **c. Timepoint decoding accuracy as a function of order: eigenvector centrality.** This panel is in the same format as Panel a, but here eigenvector centrality has been used to project the high-dimensional patterns of dynamic correlations onto a lower-dimensional space. **d. Normalized timepoint decoding accuracy as a function of order: eigenvector centrality.** This panel is in the same format as Panel b, but here eigenvector centrality has been used to project the high-dimensional patterns of dynamic correlations onto a lower-dimensional space.

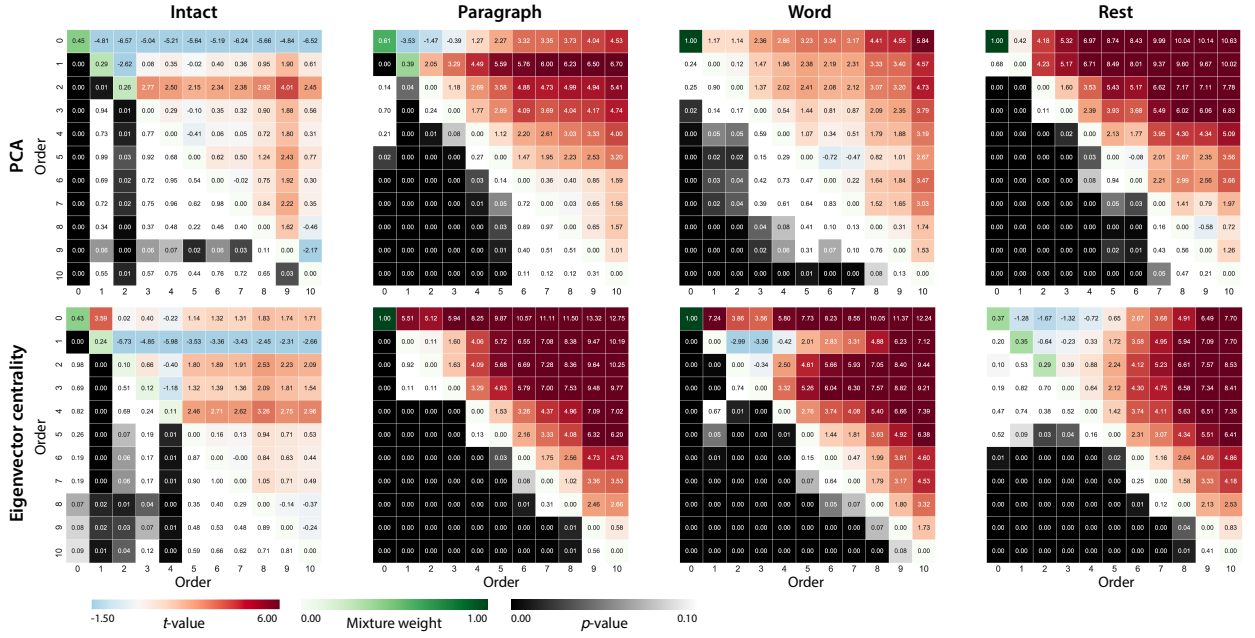


Figure 8: Statistical summary of decoding accuracies for different neural features. Each column displays decoding results for one experimental condition (intact, paragraph, word, and rest). We considered dynamic activity patterns (order 0) and dynamic correlations at different orders ($order > 0$). We used two-tailed t -tests to compare the distributions of decoding accuracies obtained using each pair of features. The distributions for each feature reflect the set of average decoding accuracies (across all kernel parameters), obtained for each random assignment of training and test groups. In the upper triangles of each map, warmer colors (positive t -values) indicate that the neural feature indicated in the given row yielded higher accuracy than the feature indicated in the given column. Cooler colors (negative t -values) indicate that the feature in the given row yielded lower decoding accuracy than the feature in the given column. The lower triangles of each map denote the corresponding p -values for the t -tests. The diagonal entries display the relative average optimized weight given to each type of feature, in a decoder that included all feature types (see *Feature weighting and testing*).

414 Both sets of temporal decoding analyses yielded qualitatively similar results for the auditory (non-rest)
415 conditions of the experiment (Fig. 7: pink, green, and teal lines; Fig. 8: three leftmost columns). The highest
416 decoding accuracy for participants who listened to the intact (unscrambled) story was achieved using high-
417 order dynamic correlations (PCA: second-order; eigenvector-centrality: fourth-order). Scrambled versions
418 of the story were best decoded by lower-order correlations (PCA/paragraph: first-order; PCA/word: order
419 zero; eigenvector centrality/paragraph: order zero; eigenvector centrality/word: order zero). The two sets
420 of analyses yielded different decoding results on resting state data (Fig. 7: purple lines; Fig. 8: rightmost
421 column). We note that while the resting state times could be decoded reliably, the accuracies were only very
422 slightly above chance. We speculate that the decoders might have picked up on attentional drift, boredom,
423 or tiredness; we hypothesize that these all increased throughout the resting state scan. The decoders might
424 be picking up on aspects of these loosely defined cognitive states that are common across individuals. The
425 PCA-based approach achieved the highest resting state decoding accuracy using order zero features (non-
426 correlational, activation-based), whereas the eigenvector centrality-based approach achieved the highest
427 resting state decoding accuracy using second-order correlations. Taken together, these analyses indicate
428 that high-level cognitive processing (while listening to the intact story) is reflected in the dynamics of high-
429 order correlations in brain activity, whereas lower-level cognitive processing (while listening to scrambled
430 versions of the story that lack rich meaning) is reflected in the dynamics of lower-order correlations and
431 non-correlational activity dynamics. Further, these patterns are associated both with the underlying activity
432 patterns (characterized using PCA) and also with the changing relative positions that different brain areas
433 occupy in their associated networks (characterized using eigenvector centrality).

434 Having established that patterns of high-order correlations are informative to decoders, we next won-
435 dered which specific networks of brain regions contributed most to these patterns. As a representative
436 example, we selected the kernel parameters that yielded decoding accuracies that best matched the average
437 accuracies across all of the kernel parameters we examined. Using Figure 7c as a template, the best-matching
438 kernel was a Laplace kernel with a width of 50 (Fig. 3d). We used this kernel to compute a single K by K
439 n^{th} -order DISFC matrix for each experimental condition. We then used Neurosynth (Rubin et al., 2017) to
440 compute the terms most highly associated with the most strongly correlated pairs of regions in each of these
441 matrices (Fig. 9; see *Reverse inference*).

442 For all of the story listening conditions (intact, paragraph, and word), we found that first- and second-
443 order correlations were most strongly associated with auditory and speech processing areas. During
444 intact story listening, third-order correlations reflected integration with visual areas, and fourth-order
445 correlations reflected integration with areas associated with high-level cognition and cognitive control,
446 such as the ventrolateral prefrontal cortex. However, during listening to temporally scrambled stories,

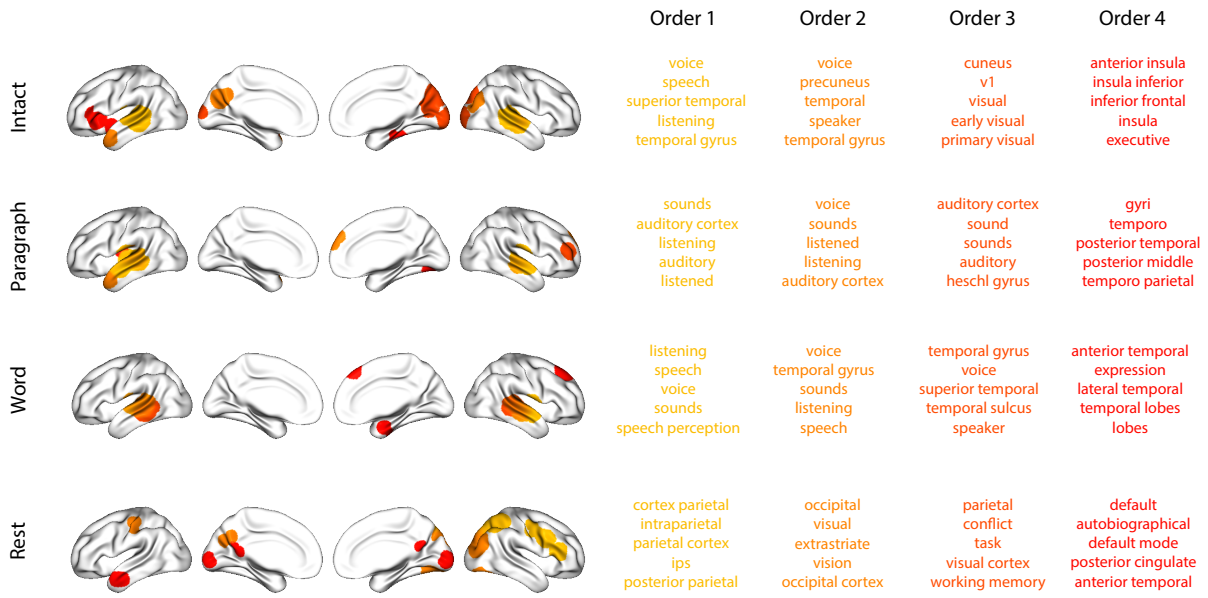


Figure 9: Top terms associated with the endpoints of the strongest correlations. Each color corresponds to one order of inter-subject functional correlations. To calculate the dynamic correlations, eigenvector centrality has been used to project the high-dimensional patterns of dynamic correlations onto a lower-dimensional space at each previous order, which allows us to map the brain regions at each order by retaining the features of the original space. The inflated brain plots display the locations of the endpoints of the 10 strongest (absolute value) correlations at each order, thresholded at 0.999, and projected onto the cortical surface (Combrisson et al., 2019). The lists of terms on the right display the top five Neurosynth terms (Rubin et al., 2017) decoded from the corresponding brain maps for each order. Each row displays data from a different experimental condition. Additional maps and their corresponding Neurosynth terms may be found in the *Supplementary materials* (intact: Fig. S1; paragraph: Fig. S2; word: Fig. S3; rest: Fig. S4).

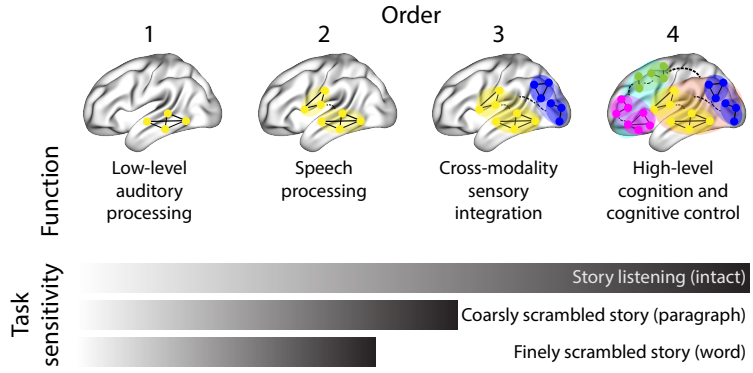


Figure 10: Proposed high-order network dynamics underlying high-level cognition during story listening. Schematic depicts higher orders of network interactions supporting higher-level aspects of cognitive processing. When tasks evoke richer, deeper, and/or higher-level processing, this is reflected in higher-order network interactions.

447 these higher-order correlations instead involved interactions with additional regions associated with speech
 448 and semantic processing. By contrast, we found a much different set of patterns in the resting state data.
 449 First-order resting state correlations were most strongly associated with regions involved in counting and
 450 numerical understanding. Second-order resting state correlations were strongest in visual areas; third-order
 451 correlations were strongest in task-positive areas; and fourth-order correlations were strongest in regions
 452 associated with autobiographical and episodic memory. We carried out analogous analyses to create maps
 453 (and decode the top associated Neurosynth terms) for up to fifteenth-order correlations (Figs. S1, S2, S3, and
 454 S4). Of note, examining fifteenth-order correlations between 700 nodes using conventional methods would
 455 have required storing roughly $\frac{700^{2 \times 15}}{2} \approx 1.13 \times 10^{85}$ floating point numbers—assuming single-precision (32
 456 bits each), this would require roughly 32 times as many bits as there are molecules in the known universe!
 457 Although these fifteenth-order correlations do appear (visually) to have some well-formed structure, we
 458 provide this latter example primarily as a demonstration of the efficiency and scalability of our approach.

459 Discussion

460 We tested the hypothesis that high-level cognition is reflected in high-order brain network dynamics (e.g.,
 461 see Reimann et al., 2017; Solomon et al., 2019). We examined high-order network dynamics in functional
 462 neuroimaging data collected during a story listening experiment. When participants listened to an auditory
 463 recording of the story, participants exhibited similar high-order brain network dynamics. By contrast,
 464 when participants instead listened to temporally scrambled recordings of the story, only lower-order brain
 465 network dynamics were similar across participants. Our results indicate that higher orders of network
 466 interactions support higher-level aspects of cognitive processing (Fig. 10).

467 The notion that cognition is reflected in (and possibly mediated by) patterns of first-order network
468 dynamics has been suggested by or proposed in myriad empirical studies and reviews (e.g., Chang &
469 Glover, 2010; Demertzi et al., 2019; Fong et al., 2019; Gonzalez-Castillo et al., 2019; Liégeois et al., 2019; Lurie
470 et al., 2018; Park et al., 2018; Preti et al., 2017; Roy et al., 2019; Turk-Browne, 2013; Zou et al., 2019). Our study
471 extends this line of work by finding cognitively relevant *higher-order* network dynamics that reflect ongoing
472 cognition. Our findings complement other work that uses graph theory and topology to characterize how
473 brain networks reconfigure during cognition (e.g., Bassett et al., 2006; Betzel et al., 2019; McIntosh & Jirsa,
474 2019; Reimann et al., 2017; Sizemore et al., 2018; Toker & Sommer, 2019; Zheng et al., 2019).

475 An open question not addressed by our study pertains to how different structures integrate incoming
476 information with different time constants. For example, one line of work suggests that the cortical surface
477 comprises a structured map such that nearby brain structures process incoming information at similar
478 timescales. Low-level sensory areas integrate information relatively quickly, whereas higher-level regions
479 integrate information relatively slowly (Baldassano et al., 2017; Chien & Honey, 2019; Hasson et al., 2015,
480 2008; Honey et al., 2012; Lerner et al., 2014, 2011). Other related work in human and mouse brains indicates
481 that the temporal response profile of a given brain structure may relate to how strongly connected that
482 structure is with other brain areas (Fallon et al., 2019). Further study is needed to understand the role of
483 temporal integration at different scales of network interaction, and across different anatomical structures.
484 Importantly, our analyses do no speak to the physiological basis of higher-order dynamics, and could reflect
485 nonlinearities, chaotic patterns, non-stationarities, or multistability, etc. However, our decoding analyses
486 do indicate that higher-order dynamics are consistent across individuals, and therefore unlikely to be driven
487 by non-stimulus-driven dynamics which are unlikely to be similar across individuals.

488 Another potential limitation of our approach relates to recent work suggesting that the brain undergoes
489 rapid state changes, for example across event boundaries (e.g., Baldassano et al., 2017). Shappell et al.
490 (2019) used hidden semi-Markov models to estimate state-specific network dynamics (also see Vidaurre et
491 al., 2018). Our general approach might be extended by considering putative state transitions. For example,
492 rather than weighting all timepoints using a similar kernel (Eqn. 4), the kernel function could adapt on a
493 timepoint-by-timepoint basis such that only timepoints determined to be in the same “state” were given
494 non-zero weight.

495 Identifying high-order network dynamics associated with high-level cognition required several impor-
496 tant methods advances. First, we used kernel-based dynamic correlations to extended the notion of (static)
497 inter-subject functional connectivity (Simony et al., 2016) to a dynamic measure of inter-subject functional
498 connectivity (DISFC) that does not rely on sliding windows, and that may be computed at individual
499 timepoints. This allowed us to precisely characterize stimulus-evoked network dynamics that were similar

500 across individuals. Second, we developed a computational framework for efficiently and scalably estimat-
501 ing high-order dynamic correlations. Our approach uses dimensionality reduction algorithms and graph
502 measures to obtain low-dimensional embeddings of patterns of network dynamics. Third, we developed
503 an analysis framework for identifying robust decoding results by carrying out our analyses using a range
504 of parameter values and then identifying which results were robust to specific parameter choices.

505 **Concluding remarks**

506 The complex hierarchy of dynamic interactions that underlie our thoughts is perhaps the greatest mystery in
507 modern science. Methods for characterizing the dynamics of high-order correlations in neural data provide
508 a window into the neural basis of cognition. By showing that high-level cognition is reflected in high-order
509 network dynamics, we have elucidated the next step on the path towards understanding the neural basis
510 of cognition.

511 **Acknowledgements**

512 We acknowledge discussions with Luke Chang, Vassiki Chauhan, Hany Farid, Paxton Fitzpatrick, Andrew
513 Heusser, Eshin Jolly, Aaron Lee, Qiang Liu, Matthijs van der Meer, Judith Mildner, Gina Notaro, Stephen
514 Satterthwaite, Emily Whitaker, Weizhen Xie, and Kirsten Ziman. Our work was supported in part by NSF
515 EPSCoR Award Number 1632738 to J.R.M. and by a sub-award of DARPA RAM Cooperative Agreement
516 N66001-14-2-4-032 to J.R.M. The content is solely the responsibility of the authors and does not necessarily
517 represent the official views of our supporting organizations.

518 **Author contributions**

519 Concept: J.R.M. Implementation: T.H.C., L.L.W.O., and J.R.M. Analyses: L.L.W.O. and J.R.M. Writing:
520 L.L.W.O. and J.R.M.

521 **References**

- 522 Allen, E. A., Damaraju, E., Plis, S. M., Erhardt, E. B., Eichele, T., & Calhoun, V. D. (2012). Tracking
523 whole-brain connectivity dynamics in the resting state. *Cerebral Cortex*, 24(3), 663–676.
- 524 Alvarez-Hamelin, I., Dall’Asta, L., Barrat, A., & Vespignani, A. (2005). *k*-corr decomposition: a tool for the
525 visualization of large scale networks. *arXiv*, cs/0504107v2.

- 526 Baldassano, C., Chen, J., Zadbood, A., Pillow, J. W., Hasson, U., & Norman, K. A. (2017). Discovering event
527 structure in continuous narrative perception and memory. *Neuron*, 95(3), 709–721.
- 528 Barthélémy, M. (2004). Betweenness centrality in large complex networks. *European Physical Journal B*, 38,
529 163–168.
- 530 Bassett, D., Meyer-Lindenberg, A., Achard, S., Duke, T., & Bullmore, E. (2006, December). Adaptive
531 reconfiguration of fractal small-world human brain functional networks. *Proceedings of the National
532 Academy of Sciences, USA*, 103(51), 19518–23.
- 533 Betzel, R. F., Byrge, L., Esfahlani, F. Z., & Kennedy, D. P. (2019). Temporal fluctuations in the brain's modular
534 architecture during movie-watching. *bioRxiv*, doi.org/10.1101/750919.
- 535 Bonacich, P. (2007). Some unique properties of eigenvector centrality. *Social Networks*, 29(4), 555–564.
- 536 Bullmore, E., & Sporns, O. (2009). Complex brain networks: graph theoretical analysis of structural and
537 functional systems. *Nature Reviews Neuroscience*, 10(3), 186–198.
- 538 Capota, M., Turek, J., Chen, P.-H., Zhu, X., Manning, J. R., Sundaram, N., ... Shin, Y. S. (2017). *Brain imaging
539 analysis kit*. Retrieved from <https://doi.org/10.5281/zenodo.59780>
- 540 Chang, C., & Glover, G. H. (2010). Time-frequency dynamics of resting-state brain connectivity measured
541 with fMRI. *NeuroImage*, 50, 81–98.
- 542 Chien, H.-Y. S., & Honey, C. J. (2019). Constructing and forgetting temporal context in the human cerebral
543 cortex. *bioRxiv*, doi.org/10.1101/761593.
- 544 Christakis, N. A., & Fowler, J. H. (2010). Social network sensors for early detection of contagious outbreaks.
545 *PLoS One*, 5(9), e12948.
- 546 Combrisson, E., Vallat, R., O'Reilly, C., Jas, M., Pascarella, A., l Saive, A., ... Jerbi, K. (2019). Visbrain: a
547 multi-purpose GPU-accelerated open-source suite for multimodal brain data visualization. *Frontiers in
548 Neuroinformatics*, 13(14), 1–14.
- 549 Comon, P., Jutten, C., & Herault, J. (1991). Blind separation of sources, part II: Problems statement. *Signal
550 Processing*, 24(1), 11 - 20.
- 551 Demertzi, A., Tagliazucchi, E., Dehaene, S., Deco, G., Barttfeld, P., Raimondo, F., ... Sitt, J. D. (2019). Human
552 consciousness is supported by dynamic complex patterns of brain signal coordination. *Science Advances*,
553 5(2), eaat7603.

- 554 Estrada, E., & Rodríguez-Velázquez, J. A. (2005). Subgraph centrality in complex networks. *Physical Review E*, 71(5), 056103.
- 555
- 556 Etzel, J. A., Gazzola, V., & Keysers, C. (2009). An introduction to anatomical ROI-based fMRI classification.
- 557 *Brain Research*, 1281, 114–125.
- 558 Fallon, J., Ward, P., Parkes, L., Oldham, S., Arnatkevičiūtė, A., Fornito, A., & Fulcher, B. D. (2019).
- 559 Timescales of spontaneous activity fluctuations relate to structural connectivity in the brain. *bioRxiv*,
- 560 doi.org/10.1101/655050.
- 561 Fong, A. H. C., Yoo, K., Rosenberg, M. D., Zhang, S., Li, C.-S. R., Scheinost, D., … Chun, M. M. (2019).
- 562 Dynamic functional connectivity during task performance and rest predicts individual differences in
- 563 attention across studies. *NeuroImage*, 188, 14–25.
- 564 Freeman, L. C. (1977). A set of measures of centrality based on betweenness. *Sociometry*, 40(1), 35–41.
- 565 Geisberger, R., Sanders, P., & Schultes, D. (2008). Better approximation of betweenness centrality. *Proceedings*
- 566 *of the meeting on Algorithm Engineering and Experiments*, 90–100.
- 567 Gershman, S., Blei, D., Pereira, F., & Norman, K. (2011). A topographic latent source model for fMRI data.
- 568 *NeuroImage*, 57, 89–100.
- 569 Gonzalez-Castillo, J., Caballero-Gaudes, C., Topolski, N., Handwerker, D. A., Pereira, F., & Bandettini, P. A.
- 570 (2019). Imaging the spontaneous flow of thought: distinct periods of cognition contribute to dynamic
- 571 functional connectivity during rest. *NeuroImage*, 202(116129).
- 572 Halu, A., Mondragón, R. J., Panzarasa, P., & Bianconi, G. (2013). Multiplex PageRank. *PLoS One*, 8(10),
- 573 e78293.
- 574 Hasson, U., Chen, J., & Honey, C. J. (2015). Hierarchical process memory: memory as an integral component
- 575 of information processing. *Trends in Cognitive Science*, 19(6), 304–315.
- 576 Hasson, U., Yang, E., Vallines, I., Heeger, D. J., & Rubin, N. (2008). A hierarchy of temporal receptive windows
- 577 in human cortex. *Journal of Neuroscience*, 28(10), 2539–2550. doi: 10.1523/JNEUROSCI.5487-07.2008
- 578 Haxby, J. V., Gobbini, M. I., Furey, M. L., Ishai, A., Schouten, J. L., & Pietrini, P. (2001). Distributed and
- 579 overlapping representations of faces and objects in ventral temporal cortex. *Science*, 293, 2425–2430.
- 580 Hinton, G. E., & Salakhutdinov, R. R. (2006). Reducing the dimensionality of data with neural networks.
- 581 *Science*, 313(5786), 504–507.

- 582 Honey, C. J., Kötter, R., Breakspear, M., & Sporns, O. (2007). Network structure of cerebral cortex shapes
583 functional connectivity on multiple time scales. *Proceedings of the National Academy of Science USA*, 104(24),
584 10240–10245.
- 585 Honey, C. J., Thesen, T., Donner, T. H., Silbert, L. J., Carlson, C. E., Devinsky, O., ... Hasson, U. (2012). Slow
586 cortical dynamics and the accumulation of information over long timescales. *Neuron*, 76, 423-434. doi:
587 10.1016/j.neuron.2012.08.011
- 588 Huth, A. G., de Heer, W. A., Griffiths, T. L., Theunissen, F. E., & Gallant, J. L. (2016). Natural speech reveals
589 the semantic maps that tile human cerebral cortex. *Nature*, 532, 453–458.
- 590 Huth, A. G., Nisimoto, S., Vu, A. T., & Gallant, J. L. (2012). A continuous semantic space describes
591 the representation of thousands of object and action categories across the human brain. *Neuron*, 76(6),
592 1210-1224.
- 593 Jutten, C., & Herault, J. (1991). Blind separation of sources, part I: An adaptive algorithm based on
594 neuromimetic architecture. *Signal Processing*, 24(1), 1–10.
- 595 Kamitani, Y., & Tong, F. (2005). Decoding the visual and subjective contents of the human brain. *Nature*
596 *Neuroscience*, 8, 679–685.
- 597 Landau, E. (1895). Zur relativen Wertbemessung der Turnierresultate. *Deutsches Wochenschach*, 11, 366–369.
- 598 Lee, D. D., & Seung, H. S. (1999). Learning the parts of objects by non-negative matrix factorization. *Nature*,
599 401, 788–791.
- 600 Lerner, Y., Honey, C. J., Katkov, M., & Hasson, U. (2014). Temporal scaling of neural responses to compressed
601 and dilated natural speech. *Journal of Neurophysiology*, 111, 2433–2444.
- 602 Lerner, Y., Honey, C. J., Silbert, L. J., & Hasson, U. (2011). Topographic mapping of a hierarchy of
603 temporal receptive windows using a narrated story. *Journal of Neuroscience*, 31(8), 2906-2915. doi: 10.1523/
604 JNEUROSCI.3684-10.2011
- 605 Liégeois, R., Li, J., Kong, R., Orban, C., De Ville, D. V., Ge, T., ... Yeo, B. T. T. (2019). Resting brain
606 dynamics at different timescales capture distinct aspects of human behavior. *Nature Communications*,
607 10(2317), doi.org/10.1038/s41467-019-10317-7.
- 608 Lin, J. (2009). Divergence measures based on the Shannon entropy. *IEEE Transactions on Information Theory*,
609 37(1), 145–151.

- 610 Lohmann, G., Margulies, D. S., Horstmann, A., Pleger, B., Lepsius, J., Goldhahn, D., ... Turner, R. (2010).
611 Eigenvector centrality mapping for analyzing connectivity patterns in fMRI data of the human brain.
612 *PLoS One*, 5(4), e10232.
- 613 Lurie, D., Kessler, D., Bassett, D., Betzel, R., Breakspear, M., Keilholz, S., ... Calhoun, V. (2018). On the
614 nature of time-varying functional connectivity in resting fMRI. *PsyArXiv*, doi.org/10.31234/osf.io/xtzre.
- 615 Mack, M. L., Preston, A. R., & Love, B. C. (2017). Medial prefrontal cortex compresses concept representations
616 through learning. *bioRxiv*, doi.org/10.1101/178145.
- 617 Mairal, J., Ponce, J., Sapiro, G., Zisserman, A., & Bach, F. R. (2009). Supervised dictionary learning. *Advances*
618 *in Neural Information Processing Systems*, 1033–1040.
- 619 Mairal, J. B., Bach, F., Ponce, J., & Sapiro, G. (2009). Online dictionary learning for sparse coding. *Proceedings*
620 *of the 26th annual international conference on machine learning*, 689–696.
- 621 Manning, J. R., Ranganath, R., Norman, K. A., & Blei, D. M. (2014). Topographic factor analysis: a Bayesian
622 model for inferring brain networks from neural data. *PLoS One*, 9(5), e94914.
- 623 Manning, J. R., Zhu, X., Willke, T. L., Ranganath, R., Stachenfeld, K., Hasson, U., ... Norman, K. A. (2018).
624 A probabilistic approach to discovering dynamic full-brain functional connectivity patterns. *NeuroImage*,
625 180, 243–252.
- 626 McInnes, L., Healy, J., & Melville, J. (2018). UMAP: Uniform manifold approximation and projection for
627 dimension reduction. *arXiv*, 1802(03426).
- 628 McIntosh, A. R., & Jirsa, V. K. (2019). The hidden repertoire of brain dynamics and dysfunction. *Network*
629 *Neuroscience*, doi.org/10.1162/netn_a_00107.
- 630 Mitchell, T., Shinkareva, S., Carlson, A., Chang, K., Malave, V., Mason, R., & Just, M. (2008). Predicting
631 human brain activity associated with the meanings of nouns. *Science*, 320(5880), 1191.
- 632 Newman, M. E. J. (2005). A measure of betweenness centrality based on random walks. *Social Networks*, 27,
633 39–54.
- 634 Newman, M. E. J. (2008). The mathematics of networks. *The New Palgrave Encyclopedia of Economics*, 2, 1–12.
- 635 Nishimoto, S., Vu, A., Naselaris, T., Benjamini, Y., Yu, B., & Gallant, J. (2011). Reconstructing visual
636 experience from brain activity evoked by natural movies. *Current Biology*, 21, 1 - 6.
- 637 Nocedal, J., & Wright, S. J. (2006). *Numerical optimization*. New York: Springer.

- 638 Norman, K. A., Newman, E., Detre, G., & Polyn, S. M. (2006). How inhibitory oscillations can train neural
639 networks and punish competitors. *Neural Computation*, 18, 1577–1610.
- 640 Opsahl, T., Agneessens, F., & Skvoretz, J. (2010). Node centrality in weighted networks: generalizing degree
641 and shortest paths. *Social Networks*, 32, 245–251.
- 642 Park, H.-J., Friston, K. J., Pae, C., Park, B., & Razi, A. (2018). Dynamic effective connectivity in resting state
643 fMRI. *NeuroImage*, 180, 594–608.
- 644 Pearson, K. (1901). On lines and planes of closest fit to systems of points in space. *The London, Edinburgh,
645 and Dublin Philosophical Magazine and Journal of Science*, 2, 559–572.
- 646 Pereira, F., Lou, B., Pritchett, B., Ritter, S., Gershman, S. J., Kanwisher, N., … Fedorenko, E. (2018). Toward
647 a universal decoder of linguistic meaning from brain activation. *Nature Communications*, 9(963), 1–13.
- 648 Preti, M. G., Bolton, T. A. W., & Van De Ville, D. (2017). The dynamic functional connectome: state-of-the-art
649 and perspectives. *NeuroImage*, 160, 41–54.
- 650 Rao, C. R. (1982). Diversity and dissimilarity coefficients: a unified approach. *Theoretical Population Biology*,
651 21(1), 24–43.
- 652 Reimann, M. W., Nolte, M., Scolamiero, M., Turner, K., Perin, R., Chindemi, G., … Markram, H. (2017).
653 Cliques of neurons bound into cavities provide a missing link between structure and function. *Frontiers
654 in Computational Neuroscience*, 11(48), 1–16.
- 655 Ricotta, C., & Szeidl, L. (2006). Towards a unifying approach to diversity measures: Bridging the gap
656 between the Shannon entropy and Rao's quadratic index. *Theoretical Population Biology*, 70(3), 237–243.
- 657 Roy, D. S., Park, Y.-G., Ogawa, S. K., Cho, J. H., Choi, H., Kamensky, L., … Tonegawa, S. (2019). Brain-
658 wide mapping of contextual fear memory engram ensembles supports the dispersed engram complex
659 hypothesis. *bioRxiv*, doi.org/10.1101/668483.
- 660 Rubin, T. N., Kyoejo, O., Gorgolewski, K. J., Jones, M. N., Poldrack, R. A., & Yarkoni, T. (2017). Decoding
661 brain activity using a large-scale probabilistic functional-anatomical atlas of human cognition. *PLoS
662 Computational Biology*, 13(10), e1005649.
- 663 Rubinov, M., & Sporns, O. (2010). Complex network measures of brain connectivity: uses and interpreta-
664 tions. *NeuroImage*, 52, 1059–1069.
- 665 Schreiber, T. (2000). Measuring information transfer. *Physical Review Letters*, 85(2), 461–464.

- 666 Shappell, H., Caffo, B. S., Pekar, J. J., & Lindquist, M. A. (2019). Improved state change estimation in
667 dynamic functional connectivity using hidden semi-Markov models. *NeuroImage*, 191, 243–257.
- 668 Simony, E., Honey, C. J., Chen, J., & Hasson, U. (2016). Dynamic reconfiguration of the default mode
669 network during narrative comprehension. *Nature Communications*, 7(12141), 1–13.
- 670 Sizemore, A. E., Giusti, C., Kahn, A., Vettel, J. M., Betzel, R. F., & Bassett, D. S. (2018). Cliques and cavities
671 in the human connectome. *Journal of Computational Neuroscience*, 44(1), 115–145.
- 672 Solomon, S. H., Medaglia, J. D., & Thompson-Schill, S. L. (2019). Implementing a concept network model.
673 *Behavior Research Methods*, 51, 1717–1736.
- 674 Spearman, C. (1904). General intelligence, objectively determined and measured. *American Journal of
675 Psychology*, 15, 201–292.
- 676 Sporns, O., & Honey, C. J. (2006). Small worlds inside big brains. *Proceedings of the National Academy of
677 Science USA*, 103(51), 19219–19220.
- 678 Thompson, W. H., Richter, C. G., Plavén-Sigray, P., & Fransson, P. (2018). Simulations to benchmark
679 time-varying connectivity methods for fMRI. *PLoS Computational Biology*, 14(5), e1006196.
- 680 Tipping, M. E., & Bishop, C. M. (1999). Probabilistic principal component analysis. *Journal of Royal Statistical
681 Society, Series B*, 61(3), 611–622.
- 682 Toker, D., & Sommer, F. T. (2019). Information integration in large brain networks. *PLoS Computational
683 Biology*, 15(2), e1006807.
- 684 Tong, F., & Pratte, M. S. (2012). Decoding patterns of human brain activity. *Annual Review of Psychology*, 63,
685 483–509.
- 686 Turk-Browne, N. B. (2013). Functional interactions as big data in the human brain. *Science*, 342, 580–584.
- 687 van der Maaten, L. J. P., & Hinton, G. E. (2008). Visualizing high-dimensional data using t-SNE. *Journal of
688 Machine Learning Research*, 9, 2579–2605.
- 689 Vidaurre, D., Abeysuriya, R., Becker, R., Quinn, A. J., Alfaro-Almagro, F., Smith, S. M., & Woolrich, M. W.
690 (2018). Discovering dynamic brain networks from big data in rest and task. *NeuroImage*, 180, 646–656.
- 691 Zar, J. H. (2010). *Biostatistical analysis*. Prentice-Hall/Pearson.
- 692 Zheng, M., Allard, A., Hagmann, P., & Serrano, M. A. (2019). Geometric renormalization unravels self-
693 similarity of the multiscale human connectome. *arXiv*, 1904.11793.

- 694 Zou, Y., Donner, R. V., Marwan, N., Donges, J. F., & Kurths, J. (2019). Complex network approaches to
695 nonlinear time series analysis. *Physics Reports*, 787, 1–97.